ADVANCED FUNCTIONAL MATERIALS
www.afm-journal.de

Catalytic Synergies in Bimetallic Ru—Pt Single–Atom Catalysts via Speciation Control

Vera Giulimondi, Andrea Ruiz–Ferrando, Adam H. Clark, Selina K. Kaiser, Frank Krumeich, Antonio J. Martín, Núria López, and Javier Pérez–Ramírez**

Bimetallic single–atom catalysts (b–SACs) have recently gained prominence by virtue of the unique catalytic cooperative interactions they can exhibit, intertwining electronic and geometric effects. To date, research efforts have exclusively focused on direct mechanisms such as electron density transfer or sequential reactivity. Herein, the first study on indirect, coordination–induced catalytic synergies in carbon-supported Ru—Pt SACs is conducted. To this end, a holistic approach is developed, combining i) precision synthesis, ii) advanced characterization, iii) exploration of single–site adsorption properties via the hydrogen evolution reaction, and iv) modeling through density functional theory. Despite the lack of both intermetallic coordination in the first or second shell and charge redistribution effects, the Ru—Pt SACs exhibit a H_2 formation rate enhanced up to 15–fold compared with their monometallic counterparts. To unfold the origin of the intermetallic cooperativity, modifications of the structural and catalytic properties induced by the integration of a second metal species are investigated. Thus, Pt atoms are found to selectively occupy the most energeticallyfavorable cavities in the support, prompting Ru atoms to assume a distinct, more active, configuration. This contribution unveils a novel principle of bimetallic cooperativity, demonstrating the key role of integrative experimental and computational analyses in studying b–SACs.

1. Introduction

Carbon–supported single–atom catalysts (SACs) have attracted considerable attention in the field of catalysis owing to their maximized metal efficiency and unique reactivity in many applications.[1,2] Nevertheless, single–metal sites present intrinsic limitations in their catalytic properties originating from the finite variety of chemical states that they can assume through coordination with functionalities in the support. To overcome this, the integration of a second metal species in the host has emerged as a compelling strategy to further expand the spectrum of SAC catalytic properties.[3–6] By virtue of metal–metal interactions, this novel class of materials, herein defined as bimetallic SACs (b–SACs), has demonstrated enhanced activity, tunable product selectivity, and superior durability for a variety of applications, including thermocatalytic, electrocatalytic and photocatalytic ones.[4,6–8] However, the intrinsic complexity of these materials poses challenges to the resolution of both the metal–site architectures and the synergistic modes of action. Metal–metal interactions do not occur exclusively in the presence of intermetallic bonds (i.e., in dimers), but also in their absence.[6] The resolution of long–range metal–metal interactions requires advanced techniques, mainly relying on X–ray absorption spectroscopy (XAS) to assess the presence of bimetallic interactions up to the second coordination shell, and density functional theory (DFT) to resolve their impact on the catalytic fingerprints of b–SACs.[3] Pioneering studies combining in–depth spectroscopic and computational

V. Giulimondi, S. K. Kaiser, F. Krumeich, A. J. Martín, J. Pérez–Ramírez
Institute for Chemical and Bioengineering
Department of Chemistry and Applied Biosciences
ETH Zurich
Vladimir–Prelog–Weg 1, 8093 Zurich, Switzerland
E-mail: jpr@chem.ethz.ch

The ORCID identification number(s) for the author(s) of this article can be found under https://doi.org/10.1002/adfm.202206513.

DOI: 10.1002/adfm.202206513

A. Ruiz–Ferrando
Departament de Química Física i Inorgànica
Universitat Rovira i Virgili
Marcel·lí Domingo s/n, 43007 Tarragona, Spain
A. Ruiz–Ferrando, N. López
Institute of Chemical Research of Catalonia (ICIQ)
The Barcelona Institute of Science and Technology
Av. Països Catalans 16, 43007 Tarragona, Spain
E-mail: nlopez@iciq.es
A. H. Clark
Paul Scherrer Institute
5232 Villigen PSI, Switzerland

analyses have reported M_1—N/O—M_2 structures (where M_1 and M_2 are chemically different metal atoms) that exhibit direct cooperative effects stemming from i) intermetallic electron density transfer, which tunes the binding energy of key intermediates, ii) sequential participation of metal sites in cascade reactions, or iii) unique reactant adsorption configurations adopted on the two metal sites that enhance the reaction kinetics.[9–11]

Nevertheless, the study of this promising class of SACs is still in its infancy. The varied and complex nature of catalytic synergies is largely unexplored and calls for a deeper understanding of the origin of the enhanced activity. Besides, atomically–precise synthesis of b–SACs remains a major challenge in this respect.[3,7] Owing to the broad distribution of compositions and anchoring sites in the carbon supports, unraveling underlying structure–property relationships is not straightforward. A reliable approach may consist in thoroughly investigating structural modifications induced by the integration of the second metal species in the synthetic strategy, affecting the coordination of the former one. Diverse metal–site configurations can exhibit both specific geometric and charge redistribution effects, which are convoluted and arduous to resolve.[3] Specifically, disentangling indirect cooperativity mechanisms (i.e., coordination–induced effects) from direct ones (e.g., electron density transfer or sequential reactivity) remains a major challenge. To this end, the integration of secondary metal atoms in monometallic SACs that are completely isolated from each other (i.e., not bridged via N/O atoms) may offer an effective strategy to assess whether the presence of direct metal–metal interactions is necessary for intermetallic cooperativity. A suitable combination may be Ru and Pt, since the two metals have been studied for diverse applications as both monometallic single atoms and bimetallic dimers on carbon supports.[2,12,13]

Herein, we conduct the first study on indirect catalytic synergies in carbon–supported b–SACs. For this purpose, spatially– and electronically–isolated Ru and Pt atoms are generated on a N–doped carbon host, as i) corroborated by the lack of intermetallic interactions in either the first or second coordination shell by in–depth XAS characterization, and ii) confirmed by DFT analysis of possible charge redistribution effects. Despite the isolated nature of the metal atoms, the Ru—Pt SACs exhibit up to 15–fold enhanced activity compared with their monometallic counterparts for the hydrogen evolution reaction (HER), which serves here as a model probe for single–site H–adsorption properties.[14,15] To unravel the origin of the cooperativity, the b–SAC structure is thoroughly studied by integrative XAS and DFT analyses. The coordination configurations of each metal species are investigated by simulating the key steps in the synthetic process, while potential geometric and electronic synergistic effects are systematically probed. As a result, the enhanced activity of the Ru—Pt SACs is attributed to the stabilization of Ru atoms in distinct cavities in the presence of Pt atoms, resulting in a close–to–neutral H–adsorption strength (i.e., the metric for high HER activity). These results expand the scope of cooperativity effects in b–SACs, evidencing that indirect coordination–induced synergistic effects should not be overlooked when studying this novel class of catalytic materials.

2. Results and Discussion

2.1. Synthetic Strategy for Isolated Ru and Pt Atoms

Carbon–supported Pt single atoms ("SA" in the sample code) are derived by simple incipient wetness impregnation of a polyaniline–derived N–doped carbon (NC) with a solution of H_2PtCl_6 dissolved in water (w), followed by thermal activation in the range of 473–1073 K (*T*, Pt SACs denoted as Pt_{SA}/NC–w–*T*, **Figure 1**; Figures S1 and S2, Supporting Information).[16] Conversely, the generation of Ru single atoms requires a strongly oxidizing agent, i.e., aqua regia (a), and mild activation temperatures (Ru SAC denoted as Ru_{SA}/NC–a–473, Figure 1; Figures S1 and S2, Supporting Information).[16] In aqueous solutions, the $RuCl_3$ precursor undergoes hydrolysis, exchanging Cl^- ligands for H_2O molecules.[17] The resulting Ru species are then reduced by surface functional groups of the carbon support, yielding Ru nanoparticles.[18] Notably, this process is hindered by the addition of H_2PtCl_6 in the aqueous solution, generating a Ru—Pt SAC (Figure 1, denoted as $[Ru—Pt]_{SA}$/NC–w–473), as visualized in HAADF–STEM and corroborated by X–ray diffraction (Figures S1 and S3, Supporting Information). This is explicable by the rapid and partial hydrolysis of H_2PtCl_6, which is capable i) of releasing Cl^- ions in water while maintaining from two to four Cl^- ligands depending on the solution pH,[19] and thus ii) of stabilizing the Ru species as single atoms on NC via a Cl–mediated oxidation mechanism.[14,20] In line with the affinity of both metal atoms for the N–functionalities in the support,[14,16] microscopy analysis evaluating the intensity profiles of Ru and Pt proximal atoms identifies interatomic distances of at least 4 Å (Figure S4, Supporting Information), suggesting full spatial isolation between the metal species.[9]

Remarkably, the stabilizing effect of Pt atoms on their Ru counterparts is preserved upon thermal activation at high temperature (yielding a Ru—Pt SAC denoted as $[Ru—Pt]_{SA}$/NC–w–1073, Figure 1; Figure S3, Supporting Information), leading to Cl^- ligand removal and subsequent Ru agglomeration in the monometallic case (Figure 1; Figure S2, Supporting Information).[16] The highly stable Pt single atoms likely block the diffusion paths of the Ru atoms that lead to the formation of Ru nanoparticles, simultaneously offering the possibility to lower the chlorination degree of Ru atoms until full depletion of Cl^- ligands (vide infra). These results demonstrate that the integration of stable metal atoms (e.g., Pt atoms) in SAC synthetic procedures is a valuable strategy to control the low nuclearity in sintering-prone metal atoms (e.g., Ru atoms) and attain distinct coordination properties compared to their monometallic counterparts.

2.2. Resolution of Metal Structure

2.2.1. Coordination Environment of Ru and Pt Atoms

The generation of isolated metal atoms in both $[Ru—Pt]_{SA}$/NC–w–473 and $[Ru—Pt]_{SA}$/NC–w–1073 is corroborated by the Fourier transform analysis of extended X–ray absorption fine structure (FT–EXAFS) spectra. No metal–metal bonds are identified, with the exception of minor Ru–Ru contributions

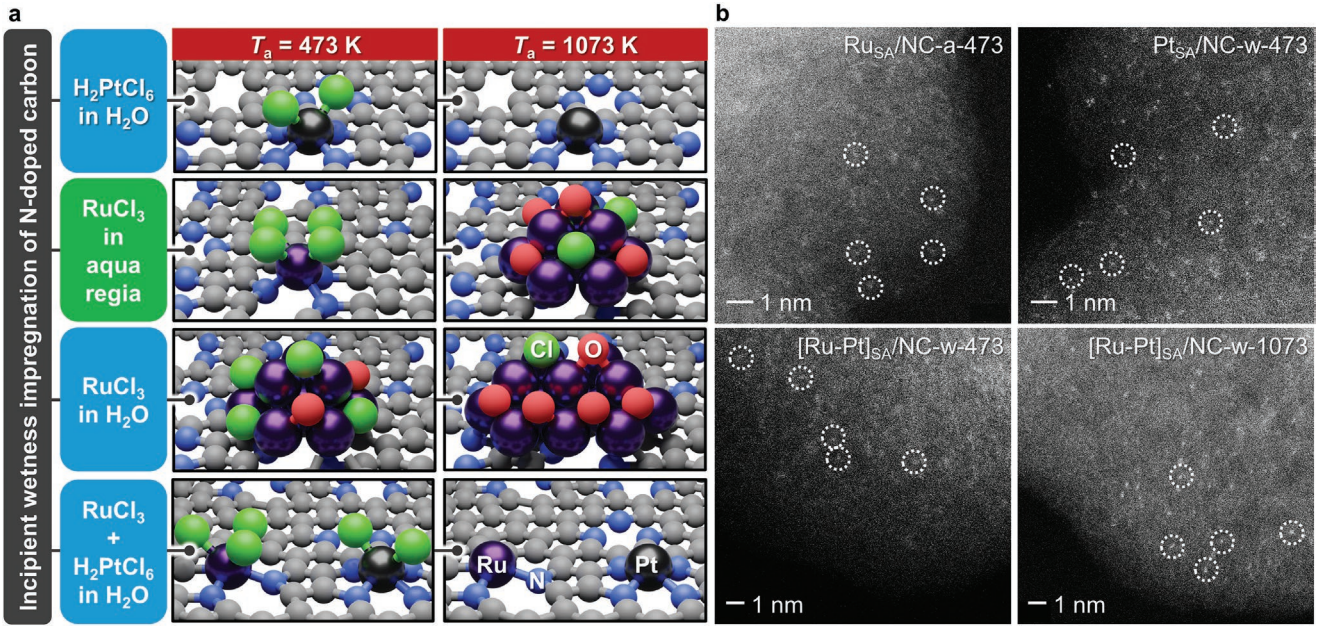

Figure 1. a) Schematic illustration of the role of synthetic parameters (i.e., solvent, presence of secondary metal precursor, and temperature of thermal activation, T_a) in controlling the nanostructure of NC–supported monometallic and bimetallic catalysts, as indicated by the structural representations. The simultaneous impregnation of NC with aqueous solutions of $RuCl_3$ and H_2PtCl_6 prevents the agglomeration of Ru single atoms into nanoparticles at both mild and high thermal activation conditions. b) HAADF–STEM images of monometallic and bimetallic SACs. The single metal atoms are highlighted by the white dotted circles.

in [Ru—Pt]$_{SA}$/NC–w–1073 (coordination number, CN = 0.5, **Figures** 2a; Figure S5 and Table S1, Supporting Information) that are assigned to few sporadic clusters observed in HAADF–STEM (Figure S3, Supporting Information). Interestingly, FT–EXAFS analysis of [Ru—Pt]$_{SA}$/NC–w–473 suggests that the presence of $RuCl_3$ in the aqueous solution does

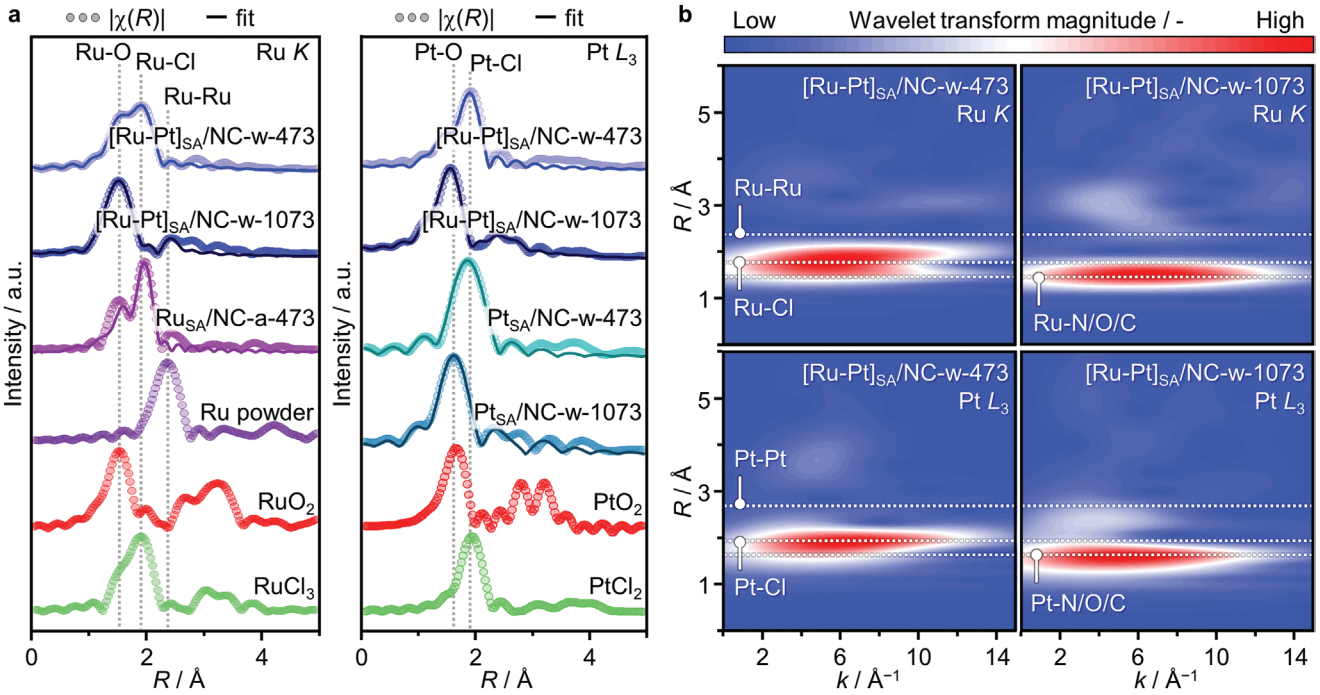

Figure 2. a) Experimental and fitted FT–EXAFS spectra in the *R*-space of monometallic and bimetallic SACs along with reference materials. b) WT–EXAFS spectra at the Ru *K* and Pt L_3 edges of the b–SACs. The absence of spectral features in the region of R = 3–5 Å and k = 9–11 Å^{-1} corroborates the spatial isolation between the Ru and Pt atoms in both samples. The characteristic lobes are marked with the corresponding contributions (namely M—M, M—Cl, and M—O).

not affect the ability of the H_2PtCl_6 to preserve the necessary Cl^- ligands for the Pt complexes to form single atoms, as indicated by a similar chlorination degree of Pt atoms in $[Ru-Pt]_{SA}$/NC–w–473 and the monometallic Pt SAC counterpart (Pt−Cl CN = 2.4 and 2.3 in $[Ru-Pt]_{SA}$/NC–w–473 and Pt_{SA}/NC–w–473, respectively, Figure 2a; Figure S5 and Table S1, Supporting Information). Conversely, the chlorinated nature of the Ru atoms in $[Ru-Pt]_{SA}$/NC–w–473 (Ru−Cl CN = 2.6, Figure 2a; Figure S5 and Table S1, Supporting Information) corroborates the Cl–mediated nature of the dispersing effect of H_2PtCl_6 on Ru species. The latter ones need Cl^- ligands to stabilize as single atoms,[14] as indicated by the strongly chlorinated character of Ru_{SA}/NC–a–473 (Ru−Cl CN = 4.3, Figure 2a; Figure S5 and Table S1, Supporting Information), which is synthesized by using aqua regia as a solvent. Full depletion of the Cl^- ligands on both metal atoms is observed upon thermal activation at 1073 K (Ru−Cl CN = 0.0 and Pt–Cl CN = 0.0, Figure 2a; Figure S5 and Table S1, Supporting Information), reflecting a stronger interaction with the NC support (Ru−N/O/C CN = 1.7 and 2.3, and Pt–N/O/C CN = 1.8 and 4.0 in $[Ru-Pt]_{SA}$/NC–w–473 and $[Ru-Pt]_{SA}$/NC–w–1073, respectively, Figure 2a; Figure S5 and Table S1, Supporting Information).

To gain further insights into the structural and electronic features of the Ru−Pt SACs, the possible presence of intermetallic interactions in the first coordination shell is assessed. Similarly to analogous NC–supported Au–Ru SACs,[14] and in line with the affinity of both metal atoms for N–functionalities,[14,16] no Ru−Pt bonds are detected in either $[Ru-Pt]_{SA}$/NC–w–473 or $[Ru-Pt]_{SA}$/NC–w–1073. Therefore, the presence of Ru−Pt dimers, and thus of direct intermetallic electron density transfer, is excluded. Nevertheless, charge redistribution effects between two foreign metal atoms may also occur by bridging N– and O–functionalities in the carbon support (i.e., when the two metal atoms are in their mutual second coordination sphere).[9,21] To this end, the wavelet transform analysis of EXAFS spectra (WT–EXAFS) constitutes a highly suitable tool to probe the presence of N/O–bridged Ru−Pt species.[3,9] In their absence, longer–range electronic interactions between Ru and Pt atoms occurring via functionalities in the carbon support could be ruled out. By comparison to the metal chloride and metal oxide standards (Figure S6, Supporting Information), and in line with the Fourier transform analysis results, $[Ru-Pt]_{SA}$/NC–w–473 presents i) M−Cl contributions, exemplified by the lobe centered at R = 1.8 Å and k = 1–10 $Å^{-1}$ at the Ru K edge and the one at R = 1.9 Å and k = 1–8 $Å^{-1}$ at the Pt L_3 edge, as well as ii) M−N/O/C contributions, exemplified by the lobe centered at R = 1.5 Å and k = 1–11 $Å^{-1}$ at the Ru K edge and the one at R = 1.7 Å and k = 1–11 $Å^{-1}$ at the Pt L_3 edge (Figure 2b). Additionally, a weak feature centered at R = 3.1 Å and k = 8–14 $Å^{-1}$ can be identified at the Ru K edge, which can be attributed to residual Ru−Cl−Ru species from the $RuCl_3$ precursor by comparison with the spectral fingerprint of the latter one (Figure S6, Supporting Information). In contrast, $[Ru-Pt]_{SA}$/NC–w–1073 shows only lobes associated to Ru−N/O/C and Pt−N/O/C contributions. Markedly, no prominent spectral features in the region of R = 3–5 Å and k = 9–11 $Å^{-1}$ can be identified in either the $[Ru-Pt]_{SA}$/NC–w–473 and $[Ru-Pt]_{SA}$/NC–w–1073. This indicates the lack of intermetallic interactions in both the first or second coordination shell, suggesting full spatial and electronic isolation between the Ru and Pt atoms.[9]

The lack of charge redistribution effects between Ru and Pt atoms is further corroborated by X–ray absorption near edge structure (XANES) analysis. In line with literature–reported studies,[3,9] intermetallic electron density transfer that may occur through the functionalities in the carbon support can be identified by comparing the white line intensity values of the bimetallic SACs to the monometallic ones. In the presence of intermetallic charge redistribution effects, i) the b–SAC spectrum of the electron–donating metal edge should present a more oxidized character than its monometallic counterpart, while ii) the b–SAC spectrum at the electron–accepting metal edge should exhibit a more reduced character than its monometallic analog.[10,22] In agreement with X–ray photoelectron spectroscopy (XPS) analysis (**Figure 3**a; Figure S7 and Tables S2–S4, Supporting Information), both metals in $[Ru-Pt]_{SA}$/NC–w–473 and $[Ru-Pt]_{SA}$/NC–w–1073 present a slightly higher white line intensity value than one of the monometallic SAC counterparts (Figure 3b). Not only does the more positively charged character of both metals in the b–SACs provide further evidence for the electronically–isolated nature of the Ru and Pt atoms, additionally corroborated by DFT analysis (vide infra), but it also suggests stronger metal–support interactions compared to the monometallic SACs. Specifically, the lesser chlorination degree of the Ru atoms in $[Ru-Pt]_{SA}$/NC–w–473 compared to Ru_{SA}/NC–a–473, reflects in the metal atom coordination sphere presenting fewer M−Cl bonds in favor of more M−N/C/O bonds (Table S1, Supporting Information). Unlike the Ru atoms, the Pt atoms in the bimetallic $[Ru-Pt]_{SA}$/NC–w–473 and the monometallic Pt_{SA}/NC–w–473 present a similar chlorination degree. Nevertheless, the more oxidized character of the Pt species likely derives from the partial Cl^- ligand transfer mechanism to the Ru ones that occurs during the b–SAC synthesis, ultimately resulting in more prominent M–N/C/O interactions (Table S1, Supporting Information). Similarly, the complete removal of Cl^- ligands in $[Ru-Pt]_{SA}$/NC–w–1073 by high thermal treatment results in a prominently stronger interaction of both metal atoms with the NC support compared to the monometallic SACs (Table S1, Supporting Information).

2.2.2. Role of Pt in Controlling Ru Speciation

The reactivity of SACs is usually rationalized by probing the catalytic properties of distinct metal–site configurations via DFT models, which are constructed on the basis of XAS analysis. Consequently, the study of b–SACs should not overlook the impact of the second metal species on the speciation of the former ones. A reliable approach consists of developing integrative theoretical models investigating i) potential intermetallic interaction occurring during the catalyst synthesis, ii) concerted adsorption of the metal species on the support, and iii) possible charge redistribution between metal centers. Accordingly, aiming to uncover the active-site structure of the Ru−Pt SACs, DFT models are developed to simulate their synthetic procedure by incipient wetness impregnation. Provided the tendency of H_2PtCl_6 to lose 2–4 Cl^- ligands in aqueous solutions, $PtCl_4$ and $RuCl_3$ species are employed as metal precursors in the DFT

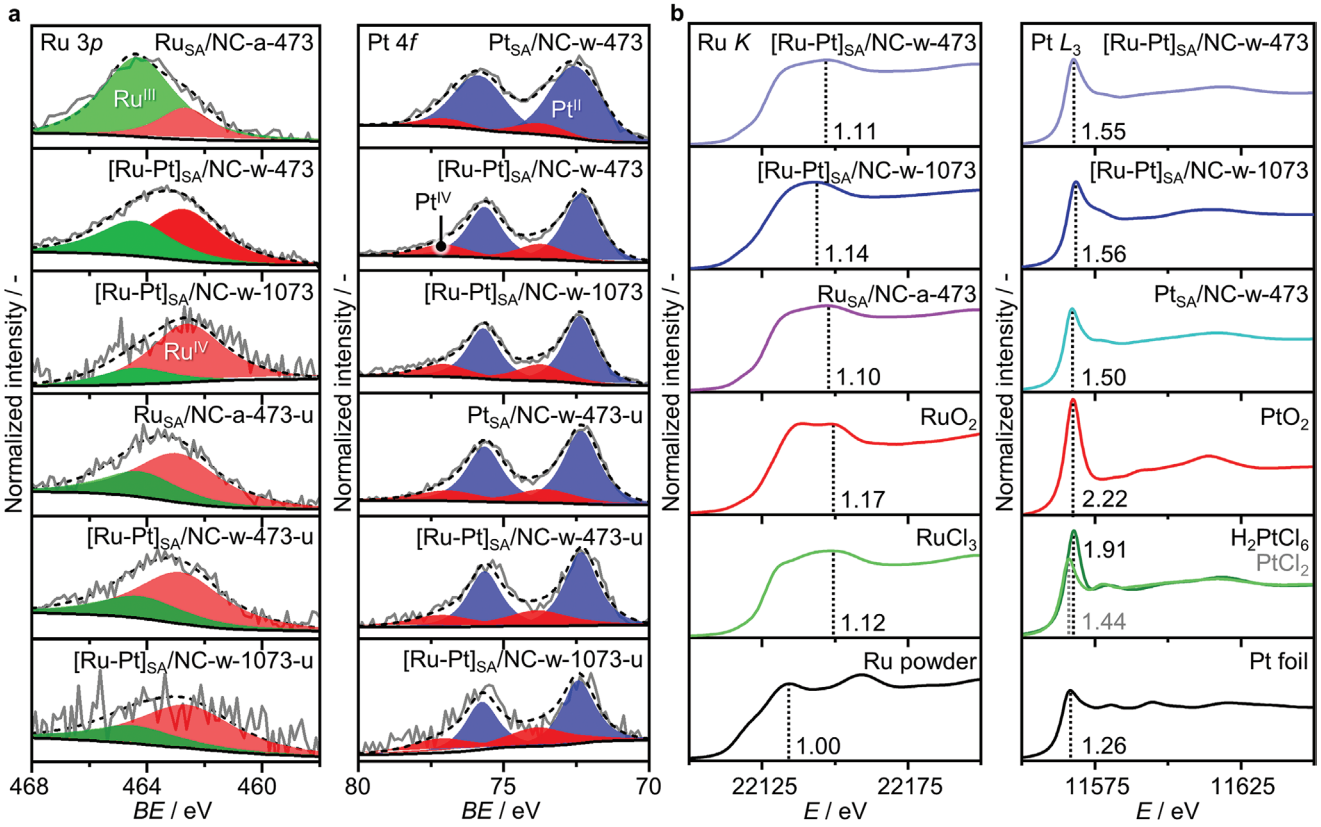

Figure 3. a) Ru 3*p* and Pt 4*f* XPS spectra of fresh and used SACs, showing the positively charged character of the catalysts. Dashed black lines represent the result of fitting the original data (solid grey lines). b) Ru *K* and Pt L_3 edge XANES spectra of monometallic and bimetallic SACs along with reference materials.

calculations. Similarly to analogous Au–Pt SACs,[20] XAS characterization of the Ru−Pt SACs suggests a Cl–mediated dispersing action of the Pt precursor on Ru species (vide supra). This is corroborated by the exothermicity of the exchange of 1–4 Cl^- ligands from the $PtCl_4$ precursor to Ru or $RuCl_x$ species (x = 0–3, Table S5, Supporting Information). To further demonstrate the key role of Cl^- ligands in preventing metal sintering, models simulating Ru complexes in aqueous solutions with varying chlorination degree, $RuCl_x(OH)_{3-x}$ (x = 0–3), are constructed to predict their tendency to deliver nanoparticles over single atoms. OH^- ligands are selected as exemplary negatively charged ligands coming from the aqueous phase to ensure neutrality among the models and remove any differential charge effects to the sintering process. Provided the i) strong affinity of Ru toward oxygenated compounds,[16] and ii) the large cohesive energy of RuO_2 (i.e., 5.0 eV per formula unit), the formation energy of RuO_2 is calculated as a function of x and compared to the binding energy of the corresponding $RuCl_x(OH)_{3-x}$ species to the NC scaffold in reference to their gas–phase species (**Figure 4**a). In line with the FT–EXAFS results, each Cl^- ligand is predicted to prevent the oxidation of Ru by at least 0.8 eV, thus hindering the formation of Ru clusters on the surface of NC. Therefore, while Ru species in an aqueous phase undergo prominent Cl^- ligand exchange for OH^- ones and are not able to preserve the necessary Cl^- ligands to form single atoms, the partial and rapid hydrolysis of H_2PtCl_6 results in a higher concentration of Cl^- ions that ultimately thwarts the ligand exchange process and yields Ru single atoms.

Having resolved the dispersing effect of the chlorinated Pt species on the Ru ones (Figure 4b), the coordination configurations of the two metal atoms are unraveled. For this purpose, the energy paths for the adsorption and dechlorination of each metal species are calculated under different thermal conditions (i.e., 473 and 1073 K). In an effort to represent the wide range of possible chemical environments in NC (Figure 4c), the energy paths are computed over a number of potential cavities in the support (Figure 4d; Figure S8 and Tables S6–S8). Among them, the 3×N5 (*t*–pyrrolic) and 4×N6 (*sq*–tetrapyridinic) cavities are selected as representatives of trigonal (*t*) and square–planar (*sq*) geometries, respectively, in agreement with literature–reported studies.[23] Owing to the out–of–plane configuration imposed by trigonal cavities, highly chlorinated species (i.e., $RuCl_3$ and $PtCl_4$) tend to adsorb on 3×N5 cavities. At 473 K, in line with the FT–EXAFS results of [Ru−Pt]/$_{SA}$NC–w–473 (Figure 2a; Table S1, Supporting Information), the adsorbed species are unlikely to undergo full dechlorination, mainly resulting in $RuCl_3$* and $PtCl_2$* configurations (–4.1 and –3.5 eV, respectively). At 1073 K, full depletion of Cl^- ligands of Pt species is hindered over trigonal cavities. This hints at the migration of PtCl* and Pt* species to 4×N6 cavities, where the full depletion of Cl^- is strongly exothermic (> 3.6 eV). Conversely, the formation of Cl–free Ru*

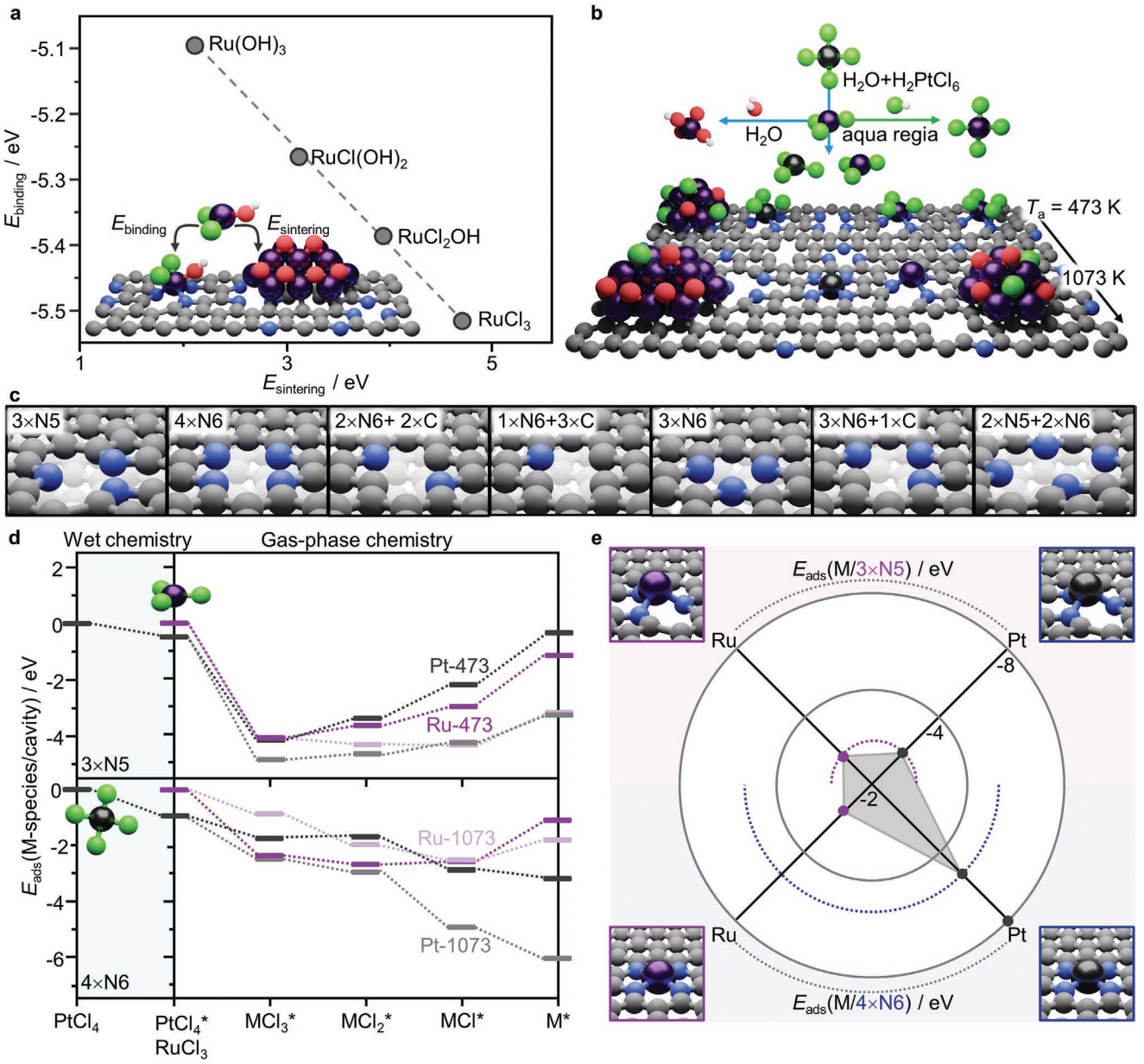

Figure 4. a) Binding energies ($E_{binding} = E(RuCl_x(OH)_{3-x}^*) - E(3\times N5) - E(RuCl_x(OH)_{3-x})_{gas}$, where $x = 0$–3) of different Ru species as a function of their sintering energy, calculated as the formation energy of RuO_2 ($E_{sintering} = E(RuO_2^*) + \frac{1}{2}E(H_2)_{gas} + x{\cdot}E(HCl)_{gas}) - E(RuCl_x(OH)_{3-x}^*) - (x-1){\cdot}E(H_2O)_{gas}$, where $x = 0$–3). As the chlorination degree of the Ru species decreases, the formation of RuO_2 is thermodynamically favored, leading to the formation of Ru NPs. b) Schematic representation of the impact of both the choice of the solvent and the presence of H_2PtCl_6 on the coordination of Ru species (i.e., Cl^- and OH^- ligands) in solution, leading to distinct metal nanostructures upon thermal activation (T_a). c) Structural representation of the set of N–cavities that are employed in the DFT models. d) Adsorption and dechlorination paths of Ru and Pt precursors on 3×N5 and 4×N6 cavities at 473 and 1073 K. e) Radar plot of the adsorption energies (E_{ads}) of Ru and Pt single atoms on 3×N5 (upper purple region) and 4×N6 cavities (lower blue region) in reference to the bulk atom and the pristine cavities. DFT simulations predict better stabilization, corresponding to a more negative E_{ads} value, i) of Ru single atoms compared to their Pt counterparts on 3×N5 cavities (as indicated by the purple dotted line) and ii) of Pt single atoms compared to their Ru counterparts on 4×N6 cavities (as indicated by the blue dotted line), prompting Ru atoms to be preferentially stabilized on 3×N5 cavities in the presence of their Pt counterparts.

species is allowed with isoenergetic configurations over both 3×N5 and 4×N6 cavities (−3.2 eV).

Notably, these energy fingerprints point to an irreversible occupation of the 4×N6 cavities by Pt atoms (−6.0 eV), while Ru atoms can be reversibly adsorbed on both and 4×N6 cavities. This leads to the preferential stabilization of Ru atoms on the 3×N5 cavities in $[Ru{-}Pt]/_{SA}NC$–w–1073 as a result of the reduced availability of free 4×N6 ones (filled by Pt atoms). Additionally, the presence of Pt atoms firmly anchored to 4×N6 cavities hinders the diffusion and agglomeration of Ru species during thermal treatment under high temperature, leading to the stabilization of Ru as single atoms. The cavity control

exerted by Pt atoms is further corroborated by the more negative adsorption energy values in reference to bulk metals for both i) Ru single atoms compared with their Pt analogs on 3×N5 cavities and ii) Pt single atoms compared with their Ru analogs on 4×N6 cavities (Figure 4e). This concerted adsorption of Ru and Pt is already expected to take place at mild activation temperatures, since a varied distribution of chlorinated and non–chlorinated Ru and Pt species is predicted to populate the surface of NC in $[Ru-Pt]_{SA}$/NC–w–473. At 1073 K, this phenomenon is maximized as full depletion of Cl^- ligands is achieved.

The DFT–predicted architectures for both the Pt and Ru atoms in $[Ru-Pt]_{SA}$/NC–w–1073 are in line with the FT–EXAFS analysis results. Specifically, the square–planar coordination of the Pt atoms on 4×N6 sites in $[Ru-Pt]_{SA}$/NC–w–1073 agrees well with the Pt–N/O/C coordination number of 4.0 identified by EXAFS analysis (Table S1, Supporting Information). For the Ru atoms, the DFT–predicted out–of–plane configuration on 3×N5 sites is corroborated by the Ru−N/O/C coordination number of 2.3 (Table S1, Supporting Information). The slightly lower value than the theoretical one of 3, can be explained by i) the averaging character of the EXAFS technique, and ii) inevitable contributions of low–coordinated metal species in edge defects or other nitrogenated sites that are also present in the NC support.[24] Furthermore, a small degree of heterogeneity in the metal species configurations, as mirrored by the presence of a short–bonding Ru−N/O/C contributions (CN = 0.4), will also contribute to minor deviations between the theoretical and experimental results. In the case of $[Ru-Pt]_{SA}$/NC–w–473, the chlorinated character of the catalyst complicates an accurate evaluation of the metal atom interaction with the support, owing to prominent M−Cl spectral features that can mask weaker M−N/O/C contributions. Furthermore, both the Ru−N and Pt−N distances of the DFT–modeled structures increase by at least 0.1 Å when a Ru or Pt atom presents two Cl^- ligands in its coordination environment (Table S9, Supporting Information). The metal atoms are vertically displaced due to the steric hindrance of the Cl^- ligands, resulting in asymmetries in the metal atom position within the 3×N5 that can yield lower M−N/O/C coordination numbers for chlorinated structures.

Upon rationalization of the metal–specific architectures, the tendency of Ru and Pt atoms to stabilize in dimeric architectures is computationally explored (Table S10, Supporting Information). In line with the FT– and WT–EXAFS analyses, the formation of dimeric species is found to be thermodynamically improbable (>1.3 eV). Having excluded the presence of intermetallic bonds, DFT models featuring Ru and/or Pt species in adjacent 3×N5 and 4×N6 cavities are constructed to probe potential intermetallic charge redistribution effects. Metal–metal distances of 4.1 and 5.9 Å were selected as the minimal possible intermetallic distances, in agreement with both EXAFS analysis, showing lack of intermetallic interactions in either the first or second coordination shells (Figure 2; Table S1, Supporting Information), and microscopy analysis of the intensity profiles of Ru and Pt proximal atoms, indicating intermetallic distances of >4 Å (Figure S4, Supporting Information). In line with the spectroscopic analysis, differences up to 0.1–0.2 eV in core–level shifts between the configurations point to the exclusive presence of electronically–isolated Ru and Pt single atoms supported on NC (**Table 1**). This evidence lays the basis for the study of catalytic fingerprints in Ru−Pt SACs that stem exclusively from coordination–induced effects.

Table 1. Differences in simulated core–level shifts and H–adsorption free energies (ΔCLS and ΔG_{H^*}, respectively, in eV) of Ru and Pt species on adjacent 3×N5 and 4×N6 cavities between monometallic and bimetallic systems.

M–M distance / Å	Configuration	ΔCLS eV^{-1}	$\Delta[\Delta G_{H^*}]$ eV^{-1}
4.1	Ru/3×N5	0.05	0.03
	Pt/3×N5	0.06	0.08
	Ru/4×N6	0.15	0.06
	Pt/4×N6	0.24	0.09
5.9	Ru/3×N5	0.00	0.06
	Pt/3×N5	0.01	0.04
	Ru/4×N6	0.00	0.07
	Pt/4×N6	0.06	0.03

2.3. Catalytic Synergies Between Isolated Ru and Pt Atoms

2.3.1. Evaluation of Single–Site H–Adsorption Properties

Following the structural identification of the Ru−Pt SACs, their catalytic fingerprints can be explored by means of hydrogen evolution reaction (HER). The single-site nature of this reaction offers a platform for the exploration of intermetallic cooperativity mechanisms between isolated metal sites. Specifically, the HER constitutes a unique probe for H–adsorption properties owing to i) the high sensitivity of the reaction kinetics to the coordination environment of the active site, together with the ii) well–established two-step mechanism and kinetic features, mirroring the catalyst H–adsorption strength.[14,15] A recent pioneering study reported outstanding catalytic synergies for the HER in carbon–supported Ru−Pt dimers, enhancing H–adsorption properties via direct electron density modulation between Ru and Pt atoms.[13] In our study, by spatially and electronically isolating the Ru and Pt atoms, we probe potential indirect modes of synergistic action. Remarkably, the Ru−Pt SACs are found to magnify the activity for the HER of their monometallic counterparts, which present similar catalytic performances, by ≈5 times in $[Ru-Pt]_{SA}$/NC–w-473 and by ≈15 times in $[Ru-Pt]_{SA}$/NC–w–1073 (**Figure 5**a; Figure S9 and Table S11, Supporting Information).

Further insights into the distinct catalytic features of the Ru−Pt SACs can be gained by analysis of the reaction kinetics. Under acidic conditions, the HER mechanism consists of an initial adsorption step of H^+ (coupled to electron transfer) onto the active site, followed by a H_2 formation step (Figure 5b).[25] According to classical electro–kinetics, under potentiostatic sweep tests (i.e., linear sweep voltammetry, LSV) the response of the reaction rate to changes in potential (i.e., Tafel analysis) can provide an indication of the rate–determining step. To this end, the evaluation of the reaction rate–potential slopes at potentials close to equilibrium (i.e., Tafel slopes) can identify the initial adsorption or the H_2 formation as the rate–determining step (corresponding to slopes of ≈120 and ≈40 mV dec^{-1},

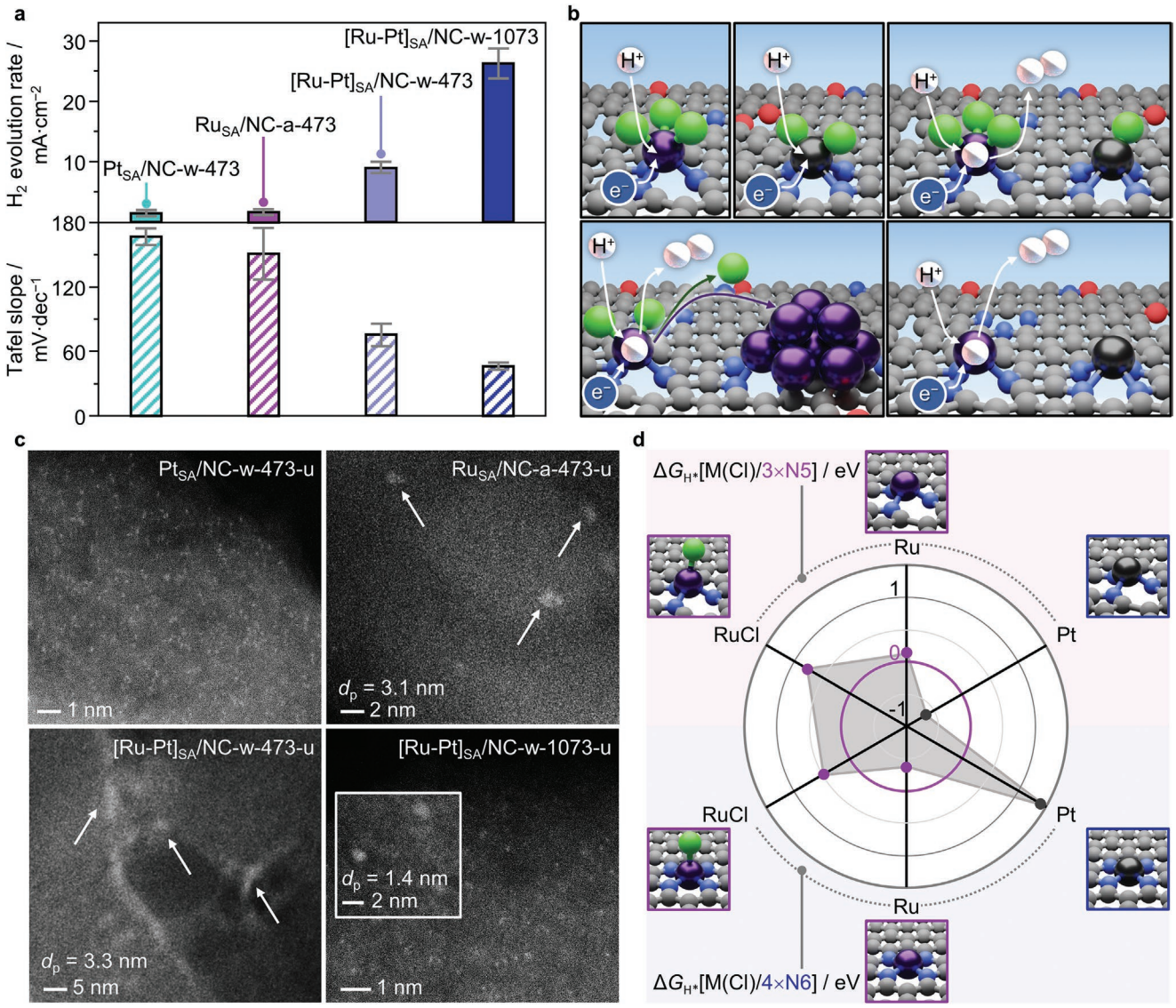

Figure 5. a) HER activity plot representing H_2 evolution rates (i.e., cathodic current densities) and Tafel slopes at –0.2 V versus RHE in 0.5 M H_2SO_4 for the monometallic and bimetallic SACs. Data presented as mean ± SD (n = 3). b) Schematic representations of the rate-determining steps in the HER mechanism of monometallic and bimetallic SACs (upper row) and together with schematic representations of the single–atom agglomeration mechanism via Cl^- ligand stripping in $[Ru-Pt]_{SA}$/NC–w–473 (lower row), which is hindered in $[Ru-Pt]_{SA}$/NC–w–1073. c) HAADF–STEM of used monometallic and bimetallic SACs at –0.2 V versus RHE in 0.5 M H_2SO_4, together with average particle sizes (d_p). d) Radar plot of H–adsorption Gibbs free energy (ΔG_{H^*}) of RuCl, Ru, and Pt species on both 3×N5 cavities (upper purple region) and 4×N6 cavities (lower blue region), accompanied by their structural representations. Cl–free Ru species on 3×N5 cavities are identified as the most active species for the HER, owing to their neutral ΔG_{H^*} value (0.09 eV).

respectively).[26] While the HER over both monometallic SACs is limited by the adsorption step, the b–SACs feature the second step as the rate–determining one (Figure 5a; Figure S10 and Table S11, Supporting Information), reflecting the enhanced H–adsorption properties. However, the similar reaction rate–potential slopes exhibited by $[Ru-Pt]_{SA}$/NC–w–473 and $[Ru-Pt]_{SA}$/NC–w–1073 may apparently contradict the significantly more prominent catalytic synergy exhibited by the latter one. This is explicable by the poisoning effect of Cl^- ligands in $[Ru-Pt]_{SA}$/NC–w–473, which results in a shift of the onset potential to more negative potentials. In line with the high chlorination degree and limited interaction with the support, $[Ru-Pt]_{SA}$/NC–w–473 and Ru_{SA}/NC–a–473 show pronounced deactivation already during a second LSV (–38.0 ± 9.0% compared to the activity in the first LSV, Figure S9 and Table S11, Supporting Information). Conversely, the Cl–free and well–anchored metal atoms in $[Ru-Pt]_{SA}$/NC–w–1073 show minor deactivation (–11.1 ± 2.6% compared to the activity in the first LSV, Figure S9 and Table S11, Supporting Information). HAADF–STEM analysis of the used catalysts (including "–u" in the sample code) shows metal–atom agglomeration into nanoparticles (average size: 3.3 nm, Figure 5c) in the former and only minor cluster formation in the latter (average size: 1.4 nm, Figure 5c). Consequently, catalyst deactivation of both $[Ru-Pt]_{SA}$/NC–w–473 and Ru_{SA}/NC–a–473 is imputed to Ru single–atom agglomeration induced by Cl^- ligand stripping upon applying a sufficiently

reducing potential (Figure 5b).[14] Hence, by displacing Ru atoms in distinct cavities (vide supra) and allowing for complete depletion of their Cl^- ligands at thermal activation conditions (i.e., 1073 K) by blocking the sintering paths of Ru atoms, the Pt species are found to exert coordination–induced promotional effect on their Ru counterparts that reflects not only in the catalyst activity for the HER but also in its stability.

2.3.2. Origin of Intermetallic Cooperativity

When two distinct single-metal atoms are present on the same support, they can either catalyze the reaction in parallel on each site or cooperatively participate in the mechanism.[27] Provided the spatial and electronic isolated nature of the Ru−Pt SACs, single–site catalytic fingerprints are first explored. The H–adsorption free energy (ΔG_{H^*}) is commonly employed as a descriptor of catalytic activities for the HER, as it follows a volcano trend where $\Delta G_{H^*} = 0$ corresponds to the highest hydrogen evolution rates.[28] Recently, this model was improved by linking microkinetics to the thermodynamic diagrams for the HER, showing that slightly more positive values ($\Delta G_{H^*} =$ 0.2 eV at $U = 0$ V) would be responsible for the current densities observed in the kinetically active region.[29] Therefore, DFT is employed to systematically evaluate the ΔG_{H^*} of all potential active site architectures (i.e., MCl_2, MCl, and M species stabilized on both trigonal and square–planar cavities, as summarized in Figure S11 and Table S12, Supporting Information).

In stark contrast with carbon–supported Pt nanoparticles, which are the state–of–the–art commercial catalysts for the HER,[30] experimental catalytic tests of Pt SACs show modest activity. This can be assigned to the DFT–predicted square–planar geometry of Pt species (vide supra). Owing to their weak H–adsorption strength ($\Delta G_{H^*} = 1.37$ and >2.00 eV for Pt* and PtCl*, respectively, Figure 5d; Figure S11 and Table S12, Supporting Information), the reaction kinetics of the Pt SACs is limited by the H–adsorption step (Figure 5a; Figure S10, Supporting Information). Similarly, in line with the Tafel analysis (Figure 5a; Figure S10, Supporting Information), chlorinated Ru species stabilized on trigonal cavities that likely populate the monometallic Ru SAC (vide supra) also exhibit weak H–adsorption strength ($\Delta G_{H^*} = 0.7$ eV for both RuCl* and $RuCl_2$*). Consequently, the enhanced activity of the Ru−Pt SACs cannot be attributed to either Pt species or chlorinated Ru ones. Nevertheless, the b–SACs present a lower chlorination degree of the Ru atoms, due to the use of water as a solvent instead of aqua regia in the synthetic procedure. Mild thermal activation conditions likely result in a varied distribution of chlorinated and non–chlorinated Ru species in $[Ru-Pt]_{SA}$/NC–w–473, while full depletion of Cl^- ligands is achieved in $[Ru-Pt]_{SA}$/NC–w–1073. Notably, Cl–free Ru species stabilized on 3×N5 cavities exhibit a close–to–neutral ΔG_{H^*} (i.e., 0.1 eV). Contrary to their analogs on 3×N5 cavities, Cl–free Ru species on 4×N6 cavities exhibit a too strong adsorption strength ($\Delta G_{H^*} = -0.4$ eV), which disqualifies them as plausible active sites. This result exemplifies the key role of Pt species, occupying the 4×N6 cavities, in prompting the Ru ones to assume trigonal configurations that are more active for the HER. The abundancy of these species in $[Ru-Pt]_{SA}$/NC–w–1073 reflects in a 15–fold increased activity with respect to the monometallic SACs, while $[Ru-Pt]_{SA}$/NC–w–473, presenting fewer Cl–free Ru species on 3×N5 cavities, exhibits a less pronounced activity enhancement (i.e., five–fold increase).

In an effort to maximize the population of Ru atoms on 3×N5 sites, the Pt loading is varied while the Ru loading is kept constant (i.e., 0.5 wt.%). Nevertheless, the prerequisite for the stabilization of Ru single atoms over 3×N5 sites is the prevention of the metal sintering, which is achieved by virtue of the Cl–mediated dispersing effect exerted by the Pt species during the catalyst synthetic process (vide supra). In line with this, the synthesis of a Ru−Pt catalyst featuring a lower Pt loading (i.e., 0.25 wt.%, sample code: $[Ru_{0.5}–Pt_{0.25}]_{SA+NP}$/NC–w–1073) leads to the formation of Ru NPs, as visualized by HAADF–STEM analysis (Figure S12, Supporting Information). Conversely, a higher loading of Pt species (i.e., 1 wt.%, sample code: $[Ru_{0.5}–Pt_1]_{SA}$/NC–w–1073) results in atomic dispersion for both metals (Figure S12, Supporting Information). While the $[Ru_{0.5}–Pt_1]_{SA}$/NC–w–1073 exhibit similar synergistic effects to $[Ru-Pt]_{SA}$/NC–w–1073 (12–fold and 15–fold enhancement in the activity with respect to the monometallic SAC counterparts, respectively), a slight reduction in prominence of the cooperativity mechanism is observed (Figure S9, Supporting Information). We speculate that by increasing the Pt loading, the Pt atoms will progressively occupy more 3×N5 sites. As a result, their availability to Ru species will be reduced, and the Ru atoms will adopt less stable and less active configurations. We conclude that the maximization of the 3×N5 site–stabilized Ru atoms is a complex endeavor that requires an optimal Pt loading, which should be neither too low to avoid the formation of Ru NPs nor too high to prevent occupation not only of the 4×N6 sites but also of the 3×N5 ones. While this endeavor goes beyond the scope of this contribution, achieving fine control over the metal species population would be of key importance for practical applications.

Upon resolving how the integration of Pt atoms affects the configuration and H–adsorption properties of Ru atoms, diverse cooperativity mechanisms are systematically studied. First, possible direct synergistic actions are explored, including potential intermetallic charge redistribution effects. In line with the XAS analysis, differences up to 0.1 eV in the ΔG_{H^*} between models featuring Ru and/or Pt species in adjacent 3×N5 and 4×N6 cavities corroborate the lack of electron transfer between the metal atoms (Table 1, Supporting Information). Furthermore, a direct cascade mechanism is investigated. The process can be described as consisting of two consecutive steps: i) a water dissociation in one site, leading to the adsorption of H* and a free OH^- and ii) the transfer of a proton from a second water molecule to the free OH^- species with the subsequent adsorption of the remaining OH* on the other metal site. Driven by the dissociative adsorption of water on Ru atoms stabilized on 3×N5 cavities (–0.7 eV, Table S13, Supporting Information), which leads to the formation of H*−Ru−OH* centers, proton shuttle effects are probed over neighboring Pt atoms (**Figure 6**a). However, the endothermicity of water adsorption (0.8 eV) and dissociation (>2.0 eV) over square–planar Pt excludes this kind of cooperativity interactions between the Ru and Pt atoms (Table S13, Supporting Information).

Henceforth, indirect synergistic effects are explored. Seeking for large–scale configurational effects at the water–catalyst

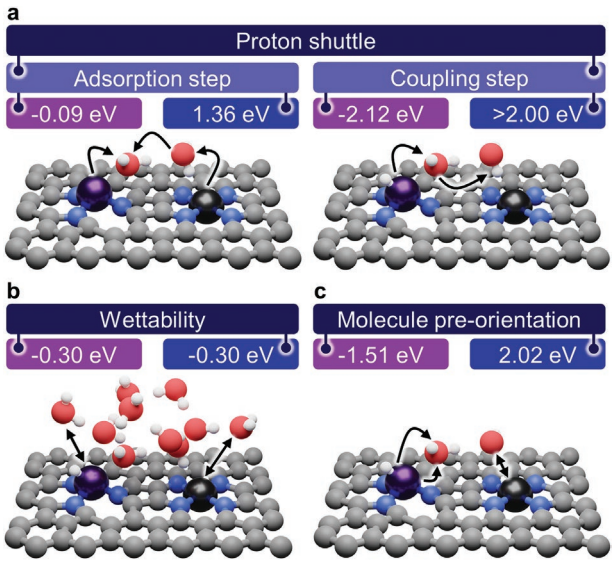

Figure 6. Schematic illustration of diverse potential synergistic effects for the HER arising between isolated Ru and Pt atoms on NC under reaction conditions, accompanied by the reaction energy of the corresponding process on the monometallic Ru SAC (purple) and the bimetallic Ru−Pt SAC (blue). a) Proton shuttle reaction mechanism, which can be described as consisting of two consecutive processes: i) a water dissociation in one site, leading to the adsorption of H* and a free OH^- and ii) the transfer of a proton from a second water molecule to the free OH^- species with the subsequent adsorption of the remaining OH* on the other metal site. b) Wettability effects, originating from the distinct interaction of a layer of water molecules in monometallic and bimetallic SACs. c) Molecule pre–orientation effects, accounting for the influence of the interaction of two water molecules in the dissociation energy to give H*−M−OH* species.

interface, the interaction of a layer of water molecules with the surface of monometallic Ru and bimetallic SACs is analyzed. Nevertheless, despite the distinct configuration that water molecules adopt over Ru and Pt atoms (O– and H–oriented, respectively), no differences are observed between the monometallic and bimetallic SACs (Figure 6b). The role of the H–oriented configuration of water molecules adsorbed on Pt atoms on 4×N6 cavities in forming H*−M−OH* species is further studied (Figure 6c). As the energy for the dissociation of water in the Ru−Pt SAC increases by 3.5 eV with respect to the monometallic Ru SAC, no improvement of the configurational disorder is identified upon integration of the Pt atoms. These results evidence the cavity control exerted by Pt atoms over Ru ones as the only effect leading to catalytic synergies.

3. Conclusion

In summary, we explored indirect catalytic synergies in bimetallic b–SACs, stemming exclusively from metal–site configuration effects. To avoid direct intermetallic charge transfer or sequential participation in cascade mechanisms, isolated Ru and Pt atoms (with intermetallic distance >4 Å) were generated on N–doped carbon by a simple dry impregnation synthetic strategy, where the formation of Ru nanoparticles was hindered by a remarkable dispersing effect of Pt species on the Ru ones. The lack of intermetallic coordination, as well as electron density redistribution, was confirmed by microscopic, spectroscopic, and DFT analyses. By investigating the catalytic fingerprints via the HER, employed as probe for H-adsorption properties of single–metal sites, cooperativity effects in the Ru−Pt SACs were unveiled, leading up to 15–fold enhanced activity. The development of an integrative approach combining spectroscopic and computational techniques proved key to unfold the role of the b–SAC synthetic strategy in controlling the metal–site configurations and exclude different potential geometric and electronic synergistic effects for the HER. Thereby, a novel principle of intermetallic cooperativity action was unraveled. Owing to the occupation of the most energetically–favorable cavities in the support by the Pt atoms, the Ru ones are induced to adopt distinct and more active configurations. Finally, our contribution shows that metal–metal interactions are not necessary for intermetallic cooperativity mechanisms to occur. As a result, prior investigating catalytic properties, the study of b–SACs should encompass a thorough analysis of the metal–coordination environment that is determined in the synthetic process. Only in this way potential coordination–induced synergistic effects can be assessed, an undertaking that is pivotal for a clear mechanistic understanding of complex metal–metal and metal–host interactions in b–SACs.

4. Experimental Section

Catalyst Preparation: The N–doped carbon support (NC) was prepared in a two–step synthesis, consisting of an oxidative polymerization of aniline and a subsequent carbonization step.[24] Aniline (50 mmol, Acros, 99.5%) was dissolved in deionized water (40 cm^3, pH 0.4; adjusted by hydrochloric acid, 1.25 M, Sigma–Aldrich, >37%) at room temperature, cooled to 277 K, and subsequently added to a precooled solution (277 K) of ammonium persulfate (50 mmol, Acros, 98%) in deionized water (20 cm^3). After 5 min of vigorous manual stirring, the mixture was kept at room temperature for 24 h to complete the polymerization process. The formed polyaniline was thoroughly washed with deionized water for neutralization, dried in vacuum at 393 K for 12 h, and afterward treated at 1073 K (heating rate 5 K min^{-1}, hold time 1 h, static N_2). The obtained N–doped carbon, having a N–content of 9.7 wt.% and a total surface area of S_{BET} = 517 m^2 g^{-1}, was ground and sieved (particle size 0.4–0.6 mm). All metal–based catalysts were prepared via an incipient wetness impregnation method with a nominal metal loading of 1 wt.%. The metal precursors, $RuCl_3{\cdot}xH_2O$ (ABCR, 99.9%, 40.0 wt.% Ru) and $H_2PtCl_6{\cdot}xH_2O$ (ABCR, 99.9%, 40.0 wt.% Pt), were dissolved in water or aqua regia (1.5 cm^3 g^{-1}), and the obtained solutions were added dropwise to the NC support. Subsequently, the samples were dried at 473 or 1073 K, as specified in the sample code, (heating rate 5 K min^{-1}, hold time 12 h, static air) to yield the respective monometallic single–atom catalysts, denoted as **Ru_{SA}/NC–a–473** and **Pt_{SA}/NC–a–473**, if aqua regia used as the solvent, or Ru nanoparticle and Pt single–atom catalysts, denoted as **Ru_{NP}/NC–w–473, Ru_{NP}/NC–w–1073** and **Pt_{SA}/NC–w–473**, **Pt_{SA}/NC–w–1073**, respectively, if water was used as the solvent. The bimetallic catalysts, denoted as **$[Ru{-}Pt]_{SA}$/NC–w–473** and **$[Ru{-}Pt]_{SA}$/NC–w–1073**, were obtained by impregnation of the NC support with an aqueous solution containing both metal precursors with a 1:1 Ru:Pt weight ratio, keeping the total metal loading at 1 wt.%. In the case of $[Ru{-}Pt]_{SA}$/NC–w–1073, the Pt loading was varied (i.e., 0.25 and 1 wt.%) while keeping the Ru metal loading constant (i.e., 0.5 wt.%) as indicated in the sample code **$[Ru_{0.5}–Pt_{0.25}]_{SA+NP}$/NC–w–1073** and **$[Ru_{0.5}–Pt_1]_{SA}$/NC–w–1073**, respectively, presenting single atoms and/or nanoparticles as indicated by the subscript. Used catalysts are indicated with "**–u**".

Catalyst Characterization: Powder X–ray diffraction (XRD) was measured using a PANalytical X'Pert PRO–MPD diffractometer with Cu–Kα radiation (λ = 1.54060 Å). The data was recorded in the

10–70°2θ range with an angular step size of 0.017° and a counting time of 0.26 s per step. Scanning transmission electron microscopy (STEM) images with a high-angle annular dark-field (HAADF) detector were acquired on an aberration–corrected HD2700CS (Hitachi) microscope operated at 200 kV. Samples were prepared by dipping the copper grid supporting a holey carbon foil in a suspension of the solid in ethanol and subsequent drying in air. X–ray fluorescence (XRF) spectroscopy, was conducted using an Orbis Micro–EDXRF spectrometer equipped with a silicon drift detector and a Rh source operated at 35 kV and 800 µA. The weight percentage of impurities (Mg, Ca, P, Mn, Fe, Ni, and Cu) was found to be at least 20 times lower than the concentration of Ru or Pt. X–ray photoelectron spectroscopy (XPS) spectra were acquired on a Physical Electronics Quantera SXM instrument using monochromatic Al–Kα radiation, generated from an electron beam operated at 15 kV, and equipped with a hemispherical capacitor electron–energy analyzer. The samples were analyzed at an electron take–off angle of 45° and a constant analyzer pass energy of 55 eV for the fresh samples, and a constant analyzer pass energy of 69 eV for the used catalysts. The detection of the metal signals in the used catalysts required a higher pass energy to increase the intensity of the signal, since the signal intensity was reduced by the presence of fluorine in the Nafion–based ink in which catalysts were embedded (vide infra). The Ru 3*p* and Pt 4*f* spectra were fitted by mixed Gaussian–Lorentzian component profiles after Shirley background subtraction. The selected peak positions are based on literature–reported data and fixed with an error of ± 0.2 eV. The detailed fitting parameters are given in Tables S3 and S4 (Supporting Information). X–ray absorption fine structure (XAFS) measurements were carried out at the SuperXAS beamline of the Swiss Light Source.[32] The incident photon beam was provided by a 2.9 T superbend magnet and subsequently collimated using a Pt–coating (for the Ru *K* edge) and a Rh–coating (for the Pt L_3 edge). The X–ray beam is then energy selected by a liquid nitrogen–cooled Si (111) channel–cut Quick–EXAFS monochromator.[31] The rejection of higher harmonics and focusing was achieved with a Pt–coating (for the Ru *K* edge) and a Rh–coating (for the Pt L_3 edge), respectively, at 2.5 mrad. The beamline was calibrated using the respective metal foils. The area of sample illuminated by the X–ray beam was 1.0 mm×0.2 mm. All spectra were recorded in transmission mode at room temperature. The extended X–ray absorption fine structure (EXAFS) spectra were acquired with a 1 Hz frequency (0.5 s per spectrum) and then averaged over 5 min. The resulting raw data were processed using the ProQEXAFS software,[33] and the EXAFS spectra were analyzed using the Demeter software.[34]

Catalytic Evaluation: The electrocatalytic hydrogen evolution reaction (HER) measurements were performed using a three–electrode cell. A glassy carbon rotating–disk electrode (0.1956 cm^2) was used as the working electrode (Pine Instruments), a standard single junction silver/silver chloride electrode as the reference electrode (3 M, Pine Instruments), and a graphite electrode as the counter electrode. An ink made of 5 mg of the catalysts, 1.6 cm^3 of ultrapure water, 0.4 cm^3 of isopropanol, and 0.04 cm^3 Nafion (5% solution, Sigma–Aldrich), sonicated for 10 min, was prepared, and 0.015 cm^3 of the ink were cast–dropped onto the RDE. The linear sweep voltammetries (LSVs) were recorded in a N_2–saturated 0.5 M H_2SO_4 electrolyte by sweeping the applied potential between 0.4 and –0.2 V versus RHE at a scan rate of 0.05 V s^{-1}, while rotating the working electrode at 1800 rpm to favor the removal of H_2 gas bubbles. The catalyst sample size (*n*) and the catalyst activity parameters, together with their standard deviation (SD) values, are reported in the (Table S11, Supporting Information).

Computational Methods: Density functional theory (DFT) on models of the Ru and Pt single atoms representing the different monometallic and bimetallic SACs was employed as implemented in the Vienna ab initio Simulation Package (VASP 5.4.4).[35] The generalized gradient approximation of the Perdew–Burke–Ernzerhof functional (GGA–PBE)[36] was used to obtain the exchange-correlation energies with dispersion contributions introduced via Grimme's DFT–D3 approach.[37] Projector augmented wave (PAW)[38] and plane waves with a cut–off energy of 450 eV, with spin polarization allowed when needed, were chosen to represent the inner electrons and the valence monoelectronic states, respectively. For the simulation of the NC support, a two–layer (6×6) slab of graphitic carbon separated by 15 Å of vacuum was used and sampled through a gamma–centered grid of 3×3×1 of *k*–points. The arising dipole was corrected in all slab models.[39] To represent the wide range of possible chemical environments in NC,[23] a set of seven cavities was constructed, comprising trigonal (*t*) and square–planar (*sq*) configurations with pyridinic and/or pyrrolic nitrogens: i) 3×N6 (*t*–tripyridinic), ii) 3×N5 (*t*–tripyrrolic), iii) 4×N6 (*sq*–tetrapyridinic), iv) 3×N6+1×C (*sq*–tripyridinic), v) 2×N6 + 2× C(*sq*–bipyridinic), vi) 1×N6+3×C (*sq*–monopyridinic), and vii) 2×N5+2 N6 (*sq*–tetrapyrrolic/ pyridinic). Single–atom catalysts were modeled by placing $PtCl_4$ and $RuCl_3$ at the center of the distinct NC cavities, with subsequent removal of chlorine to the solvent or gas–phase reservoir. The corresponding dechlorination paths were explored at 473 and 1073 K, and the core–level shifts of the resulting species were calculated. To predict the formation of Ru single atoms based on the ligands of the Ru species in the solvent (i.e., water or aqua regia), $RuCl_x(OH)_{3-x}$ (x = 0–3) species were placed at the center of the 3×N5 cavity, and the subsequent adsorption energy was calculated versus the reaction energy associated to sintering, modeled as the formation of RuO_2. Gas–phase molecules were optimized in a box of 14.0×14.5×15.0 $Å^3$. For all investigated systems, structures were relaxed using convergence criteria of 10^{-4} and 10^{-5} eV for the ionic and electronic steps, respectively. For the Gibbs free energy on the dechlorination paths, entropic contributions from molecules were considered, while for the calculation of the hydrogen Gibbs free adsorption energies at overpotential U = 0 V, entropic contributions from both molecules and slabs were accounted.

The experimental and computational datasets are made available through Zenodo at https://doi.org/10.5281/zenodo.6929058 and ioChem–BD[40] at http://doi.org/10.19061/iochem-bd-1-247, respectively.

Statistical Analysis: The data analysis for all techniques that are presented and discussed in this article is reported in the Supporting Information (Table S14, Supporting Information).

Supporting Information

Supporting Information is available from the Wiley Online Library or from the author.

Acknowledgements

V.G. and A.R.–F. contributed equally to this work. This publication was created as part of NCCR Catalysis (180544), a National Centre of Competence in Research funded by the Swiss National Science Foundation. A.R.–F. acknowledges funding from the Generalitat de Catalunya and the European Union under Grant 2021FI_B 00109. The authors thank the Scientific Centre for Optical and Electron Microscopy at the ETH Zürich, ScopeM, and the SuperXAS beamline at PSI, for access to their facilities. The Spanish Ministry of Science and Innovation is acknowledged for financial support (RTI2018–101394–B–I00 and Severo Ochoa Grant MCIN/AEI/10.13039/501100011033 CEX2019–000925–S) and the Barcelona Supercomputing Center–Mare Nostrum (BSC–RES) for providing generous computer resources.

Open access funding provided by Eidgenossische Technische Hochschule Zurich.

Conflict of Interest

The authors declare no conflict of interest.

Data Availability Statement

The data that support the findings of this study are openly available in Zenodo at https://doi.org/10.5281/zenodo.6929058 and ioChem BD at https://doi.org/10.19061/iochem-bd-1-247, reference number 41.

Keywords

active site coordination, bimetallic systems, cooperativity effects, single–atom catalysts

Received: June 8, 2022
Revised: August 13, 2022
Published online: September 14, 2022

[1] a) A. Wang, J. Li, T. Zhang, *Nat. Rev. Chem.* **2018**, *2*, 160; b) B. Bayatsarmadi, Y. Zheng, A. Vasileff, S. Z. Qiao, *Small* **2017**, *13*, 1700191; c) M. B. Gawande, P. Fornasiero, R. Zbořil, *ACS Catal.* **2020**, *10*, 2231.
[2] X. Li, L. Liu, X. Ren, J. Gao, Y. Huang, B. Liu, *Sci. Adv.* **2020**, *6*, eabb6833.
[3] J. Shan, C. Ye, Y. Jiang, M. Jaroniec, Y. Zheng, S. Z. Qiao, *Sci. Adv.* **2022**, *8*, eabo0762.
[4] Y. Ying, X. Luo, J. Qiao, H. Huang, *Adv. Funct. Mater.* **2020**, *31*, 2007423.
[5] B. Singh, V. Sharma, R. P. Gaikwad, P. Fornasiero, R. Zbořil, M. B. Gawande, *Small* **2021**, *17*, 2006473.
[6] A. Pedersen, J. Barrio, A. Li, R. Jervis, D. J. L. Brett, M. M. Titirici, I. E. L. Stephens, *Adv. Energy Mater.* **2021**, *12*, 2102715.
[7] X. Zheng, B. Li, Q. Wang, D. Wang, Y. Li, *Nano Res.* **2022**, *15*, 7806.
[8] Z. Liang, L. Song, M. Sun, B. Huang, Y. Du, *Sci. Adv.* **2021**, *7*, eabl4915.
[9] Y. Yang, Y. Qian, H. Li, Z. Zhang, Y. Mu, D. Do, B. Zhou, J. Dong, W. Yan, Y. Qin, L. Fang, R. Feng, J. Zhou, P. Zhang, J. Dong, G. Yu, Y. Liu, X. Zhang, X. Fan, *Sci. Adv.* **2020**, *6*, eaba6586.
[10] J. Fu, J. Dong, R. Si, K. Sun, J. Zhang, M. Li, N. Yu, B. Zhang, M. G. Humphrey, Q. Fu, J. Huang, *ACS Catal.* **2021**, *11*, 1952.
[11] T. Cui, Y. P. Wang, T. Ye, J. Wu, Z. Chen, J. Li, Y. Lei, D. Wang, Y. Li, *Angew. Chem.* **2022**, *61*, e202115219.
[12] a) X. Liu, Y. Jiao, Y. Zheng, K. Davey, S. Z. Qiao, *J. Mater. Chem. A* **2019**, *7*, 3648; b) X. Li, X. Yang, Y. Huang, T. Zhang, B. Liu, *Adv. Mater.* **2019**, *31*, 1902031.
[13] L. Zhang, R. Si, H. Liu, N. Chen, Q. Wang, K. Adair, Z. Wang, J. Chen, Z. Song, J. Li, M. N. Banis, R. Li, T. K. Sham, M. Gu, L. M. Liu, G. A. Botton, X. Sun, *Nat. Commun.* **2019**, *10*, 4936.
[14] V. Giulimondi, S. K. Kaiser, A. J. Martín, S. Büchele, F. Krumeich, A. H. Clark, J. PérezRamírez, *Small* **2022**, *18*, 2200224.
[15] F. C. Østergaard, A. Bagger, J. Rossmeisl, *Curr. Opin. Electrochem.* **2022**, *35*, 101037.
[16] S. K. Kaiser, E. Fako, I. Surin, F. Krumeich, V. A. Kondratenko, E. V. Kondratenko, A. H. Clark, N. López, J. PérezRamírez, *Nat. Nanotechnol.* **2022**, *17*, 606.
[17] a) M. J. Richardson, J. H. Johnston, T. Borrmann, *Eur. J. Inorg. Chem.* **2006**, *2006*, 2618; b) I. Povar, O. Spinu, *J. Electrochem. Sci. Eng.* **2016**, *6*, 145.
[18] X. Sun, S. R. Dawson, T. E. Parmentier, G. Malta, T. E. Davies, Q. He, L. Lu, D. J. Morgan, N. Carthey, P. Johnston, S. A. Kondrat, S. J. Freakley, C. J. Kiely, G. J. Hutchings, *Nat. Chem.* **2020**, *12*, 560.
[19] W. A. Spieker, J. Liu, J. T. Miller, A. J. Kropf, J. R. Regalbuto, *Appl. Catal. A* **2002**, *232*, 219.
[20] S. K. Kaiser, A. H. Clark, L. Cartocci, F. Krumeich, J. PérezRamírez, *Small* **2021**, *17*, 2004599.
[21] Y. Zhou, W. Yang, W. Utetiwabo, Y. M. Lian, X. Yin, L. Zhou, P. Yu, R. Chen, S. Sun, *J. Phys. Chem. Lett.* **2020**, *11*, 1404.
[22] E. Bus, J. A. van Bokhoven, *J. Phys. Chem. C* **2007**, *111*, 9761.
[23] A. J. Saadun, A. RuizFerrando, S. Büchele, D. Faust Akl, N. López, J. PérezRamírez, *J. Catal.* **2021**, *404*, 291.
[24] R. Lin, S. K. Kaiser, R. Hauert, J. PérezRamírez, *ACS Catal.* **2018**, *8*, 1114.
[25] a) A. Lasia, *Int. J. Hydrog. Energy* **2019**, *44*, 19484; b) B. E. Conway, L. Bai, *J. Electroanal. Chem. Interf. Electrochem.* **1986**, *198*, 149.
[26] T. Shinagawa, A. T. GarciaEsparza, K. Takanabe, *Sci. Rep.* **2015**, *5*, 13801.
[27] P. Serp, *Nanoscale* **2021**, *13*, 5985.
[28] E. Skúlason, V. Tripkovic, M. E. Björketun, S. Gudmundsdóttir, G. Karlberg, J. Rossmeisl, T. Bligaard, H. Jónsson, J. K. Nørskov, *J. Phys. Chem. A* **2010**, *114*, 18182.
[29] P. Lindgren, G. Kastlunger, A. A. Peterson, *ACS Catal.* **2019**, *10*, 121.
[30] N. Cheng, S. Stambula, D. Wang, M. N. Banis, J. Liu, A. Riese, B. Xiao, R. Li, T. K. Sham, L. M. Liu, G. A. Botton, X. Sun, *Nat. Commun.* **2016**, *7*, 13638.
[31] O. Muller, M. Nachtegaal, J. Just, D. Lutzenkirchen-Hecht, R. Frahm, *J. Synchrotron Radiat.* **2016**, *23*, 260.
[32] P. M. Abdala, O. V. Safonova, G. Wiker, W. van Beek, H. Emerich, J. A. van Bokhoven, J. Sa, J. Szlachetko, M. Nachtegaal, *Chimia* **2012**, *66*, 699.
[33] A. H. Clark, J. Imbao, R. Frahm, M. Nachtegaal, *J. Synchrotron Radiat.* **2020**, *27*, 551.
[34] M. Newville, *J. Synchrotron Radiat.* **2001**, *8*, 322.
[35] a) G. Kresse, J. Furthmüller, *Phys. Rev. B: Condens. Matter Mater. Phys.* **1996**, *54*, 11169; b) G. Kresse, J. Furthmüller, *Comput. Mater. Sci.* **1996**, *6*, 15.
[36] J. P. Perdew, K. Burke, M. Ernzerhof, *Phys. Rev. Lett.* **1996**, *77*, 3865.
[37] S. Grimme, J. Antony, S. Ehrlich, H. Krieg, *J. Chem. Phys.* **2010**, *132*, 154104.
[38] P. E. Blöchl, *Phys. Rev. B: Condens. Matter Mater. Phys.* **1994**, *50*, 17953.
[39] G. Makov, M. C. Payne, *Phys. Rev. B: Condens. Matter Mater. Phys.* **1995**, *51*, 4014.
[40] M. ÁlvarezMoreno, C. de Graaf, N. López, F. Maseras, J. M. Poblet, C. Bo, *J. Chem. Inf. Model* **2015**, *55*, 95.
[41] V. Giulimondi, A. Ruiz-Ferrando, A. H. Clark, S. K. Kaiser, F. Krumeich, A. J. Martín, N. López, J. Pérez-Ramírez, Catalytic Synergies in Bimetallic Ru-Pt Single-Atom Catalysts via Speciation Control, Zenodo **2022**, https://doi.org/10.5281/zenodo.6929058.
[42] López Research Group, Synergistic bimetallic Pt-Ru NC, ioChem BD, https://iochem-bd.iciq.es/browse/handle/100/39934.